# Structure and vibrational dynamics of NASICON-type $LiTi_2(PO_4)_3$

Marco Giarola,[†] Andrea Sanson,[*,‡] Frank Tietz,[*,¶] Sylke Pristat,[¶] Enkhtsetseg Dashjav ,[¶] Daniel Rettenwander,[§] Günther J. Redhammer,[§] and Gino Mariotto[*,†]

*Dipartimento di Informatica - Università degli Studi Verona, I-37134, Verona - Italy, Dipartimento di Fisica e Astronomia - Università degli Studi di Padova, I-35131, Padova - Italy, Forschungszentrum Jülich GmbH, Institute of Energy and Climate Research (IEK-1), D-52425 Jülich, Germany, and Universität Salzburg, Abteilung für Materialforschung und Kristallographie, Fachbereich Chemie und Physik der Materialien, A-5020 Salzburg, Austria*

E-mail: andrea.sanson@unipd.it; f.tietz@fz-juelich.de; gino.mariotto@univr.it

[*]To whom correspondence should be addressed

[†]Dipartimento di Informatica - Università degli Studi Verona, I-37134, Verona - Italy

[‡]Dipartimento di Fisica e Astronomia - Università degli Studi di Padova, I-35131, Padova - Italy

[¶]Forschungszentrum Jülich GmbH, Institute of Energy and Climate Research (IEK-1), D-52425 Jülich, Germany

[§]Universität Salzburg, Abteilung für Materialforschung und Kristallographie, Fachbereich Chemie und Physik der Materialien, A-5020 Salzburg, Austria

**Abstract**

In this work we were able to grow small single crystals of NASICON-type $LiTi_2(PO_4)_3$ of high quality by means of long-term annealing of polycrystalline specimens synthesized using conventional solid state reaction. A thorough study of their structural properties and vibrational dynamics was carried out by means of an integrated experimental and theoretical approach. A single crystal X-ray diffraction analysis at room temperature allowed to determine the precise crystal structure and the anisotropic displacement parameters of all atoms. In addition, all the 25 independent components of the polarizability tensor, expected on the basis of the group theory for the $LiTi_2(PO_4)_3$ crystal, were observed using polarized Raman spectroscopy in backscattering geometry on a micro-crystal, properly oriented by a micro-manipulator. Thus all the expected Raman modes have been unambiguously identified by determining both their wavenumber and symmetry throughout an accurate analysis of the spectral profiles observed in the different polarization configurations. Finally, these experimental findings were fully corroborated by the results of first-principles calculations performed to determine Raman and infrared vibrational modes.

# Introduction

In recent years, there has been a renewed interest in lithium ion-conducting solids because of their potential application as solid-state electrolytes in next generation Li batteries.[1,2] Lithium compounds based on the NASICON structure (acronym for $Na^+$ Super Ionic CONductor) are object of special interest, since they exhibit high ionic conductivity and are chemically versatile.[2–9]

Among the NASICON-type materials, $LiTi_2(PO_4)_3$ (LTP) is one of the most widely investigated.[10–19] Although its conductivity has been considered to be too low for practical applications, several studies have shown that it can be enhanced by the partial substitution of $Ti^{4+}$ ions by larger aliovalent cations modifying the bottlenecks of $Li^+$ conduction.[20–24] In contrast, other studies reported a substantial increase of the ionic conductivity of this compound by replacing $Ti^{4+}$ ions by smaller trivalent cations, resulting in the densification enhancement as well as in the increase of

charge carriers and of lithium content at grain boundaries.[25–29] In both cases the increase in ionic conductivity is mainly due to the increase of charge carriers. In addition, to a minor extent the substituted trivalent cations influence the ionic transport by steric considerations[30] and electronic polarizability.[31] As an example, the series $Li_{1+x}Al_xTi_{2-x}(PO_4)_3$ show a strong increase in conductivity with increasing $x$[25,32] as well as decreasing length of the a- and c-axis[25,33] due to the smaller $Al^{3+}$ ion and a lower electrostatic repulsion between $(Al,Ti)O_6$ octahedra. As a consequence, the bottlenecks of $Li^+$ conduction, i.e. the area of the oxygen triangles through which the $Li^+$ ions have to pass and named as T1 and T2 in Ref.[30] or B1 and B2 in Ref.,[31] slightly change their size from 4.52 and 4.62 Å$^2$ for $x = 0$ to 4.54 and 4.58 Å$^2$ for $x = 0.5$, respectively. However, so far it cannot be decided to which extent the change of the bottleneck size and the differently polarized bottleneck oxygens - due to the chemical bonding to $Al^{3+}$ or $Ti^{4+}$ - contribute to the enhanced conductivities.

The crystal structure of $LiTi_2(PO_4)_3$ was first investigated by Tran Qui *et al.*,[32] together with other members of the series $Li_{1+x}In_xTi_{2-x}(PO_4)_3$, but no detailed atomic positions were reported for the unsubstituted compound. Later the structure was refined by Aatiq *et al.*[33] using neutron diffraction on polycrystalline material and Bournar *et al.*[34] as well as Pinus et al.,[18] both using conventional X-ray diffraction on powders. To our knowledge no single crystal X-ray diffraction study was performed so far, thus preventing a fully exhaustive elucidation of the site distribution of mobile atoms. Therefore, more detailed structural investigations should be undertaken to provide deeper insights into the structure of this compound. Moreover, since the vibrational properties are extremely sensitive to small changes in the local structure of a compound, Raman spectroscopy can provide valuable insight into the site occupation in LTP-based materials and, accordingly, on the mechanism of ionic conductivity. In this regard, a large number of NASICON-type compounds, in polycrystalline form, have been investigated by infrared and Raman spectroscopy,[35–42] including LTP,[43–45] even though only one study dealt with the synthesis and characterization of LTP single crystals.[46] Despite this large number of experimental investigations, the vibrational dynamics of NASICON-type compounds are not yet fully clarified. In particular, no detailed study has been

carried out so far on the vibrational dynamics of LTP, although it represents the reference for the corresponding NASICON materials with high ionic conductivity. Accordingly, in this work we performed both an LTP crystal structure refinement by single crystal X-ray diffraction and an integrated vibrational dynamics study of LTP single crystals, consisting of polarized Raman scattering measurements and first-principles calculations. An excellent agreement was obtained between computational and experimental results.

The paper is organized as follows: experimental and computational details are given in Sec. II; Sec. III is dedicated to the experimental results and their discussion; Sec. IV to the computational results and their comparison with the experimental data; Sec. V to the conclusions.

# Experimental and computational details

## Materials and powder synthesis

Polycrystalline samples of $LiTi_2(PO_4)_3$ were synthesized using conventional solid state reaction. The stoichiometric amounts of $Li_2CO_3$ (VWR International, Belgium, 99 %), $TiO_2$ (VWR International, Belgium, 99 %) and $(NH_4)H_2PO_4$ (Merck, 99 %), plus an excess of 10 wt.% Li were mixed and homogenized in a mortar. The $TiO_2$ has first been dried at 600 °C for 6 h, all other reagents have been used directly as received. Then pellets with a diameter of 13 mm were pressed with 190 MPa and slowly heated in a Pt crucible with 20 °C/h up to 1000 °C for 6 hours in air and then cooled down to room-temperature with 50 °C/h. After this calcination step, the pellets were crushed, homogenized in a mortar and again pressed to pellets. By means of a second heat treatment the pellets were again sintered at 1000 °C for 720 h. During this period the powder particles grew to grains of nearly cubic shape with crystal edges of up to 150 $\mu$m.[47] Small single crystals were easily obtained after crushing the pellet and sieving the coarse powder. In view of both X-ray diffraction and polarized Raman scattering measurements, individual small crystals were glued on top of a quartz glass capillary (diameter 0.1 mm).

## X-ray diffraction details

Single-crystal X-ray diffraction data were collected at room temperature on a Bruker SMART APEX CCD-diffractometer. The single crystal to be measured was selected on the basis of its optical properties (sharp extinctions, regular shape and homogeneity in color). Intensity data were collected with graphite-monochromatized Mo $K_\alpha$ radiation (50 kV, 30 mA); the crystal-to-detector distance was 40 mm and the detector positioned at $-28^\circ$ $2\Theta$ using an $\omega$-scan mode strategy at four different $\phi$ positions (0°, 90°, 180° and 270°). 630 frames with $\Delta\omega$=0.3° were acquired for each run. Three-dimensional data were integrated and corrected for Lorentz-polarization and background effects using the APEX2 software.[48] Structure solution using direct methods and subsequent weighted full-matrix least-squares refinements on $F^2$ were carried out with SHELX-2012[49] as implemented in the program suite WinGX 2014.1.[50] More details about both data collection and structure refinement can be found elsewhere.[51]

## Raman spectroscopy measurements

Room-temperature polarized micro-Raman spectra of some selected small single crystals were recorded in quasi-backscattering geometry under excitation of the 514.5 nm line of a mixed Ar-Kr ion gas laser. The maximum laser power was 10 mW at the sample surface. A long-working distance objective (Olympus, with a magnification 80X) was used to focus the laser beam onto the sample surface. The scattered radiation was dispersed by a triple-monochromator (Horiba-Jobin Yvon, model T64000) equipped with holographic gratings (1800 lines/mm) and coupled to a nitrogen cooled CCD detector (1024×256 pixels). The spectral resolution was better than 0.6 $cm^{-1}$/pixel within the whole spectral range of interest. Proper orientation of the single micro-crystal, preliminarily mounted on top of a glass capillary, was carefully, although laboriously, achieved by means of a homemade micro-manipulator, with 6 degrees of freedom, operated under direct optical inspection of a color camera interfaced to the microscope objective, the same used to focus the laser beam onto the sample surface. The core of this micro-manipulator was a high angular-resolution goniometer which allowed for micrometric rotations of the single micro-crystal

under investigation around its crystallographic c-axis, easily determined for the highly anisotropic crystal structure of LTP. The advantages provided by this innovative approach exploiting the micro-manipulator to properly orient single micro-crystals were presented and discussed in recent studies carried out by the authors on microcrystalline anatase $TiO_2$ [52] and on crystalline $YPO_4$ and $ScPO_4$ orthophosphates.[53] It is worth to note that the micro-Raman spectra from the different single LTP crystals were very reproducible. Anyhow, long integration times (typically some hundreds of seconds) were necessary to get Raman spectra with a satisfactory signal-to-noise ratio. An accurate wave number calibration of the spectrometer was achieved based on the emission lines of a Ne spectral lamp.

For the polarization analysis of the Raman scattering from the LTP crystals, spectra in different symmetry configurations were obtained by matching the polarization setting (parallel or crossed) with proper orientation of the single crystal which was achieved by many micrometric roto-translation steps of the micro-crystal to align its c-axis either along or perpendicular to the direction of the electric field of the laser light incident on the sample surface. Accordingly to Porto's notation,[54] the scattering configurations are indicated as $\overline{k}_i(\overline{E}_i, \overline{E}_s)\overline{k}_s$, where $\overline{k}_i$ and $\overline{k}_s$ are the propagation directions, while $\overline{E}_i$ and $\overline{E}_s$ are the polarization directions of the incident and scattered light, respectively. Moreover, in order to have the same laser power at the sample surface, all spectra were excited without rotating the polarization direction of incident laser radiation, and the polarization setting was ensured by the scattered radiation analyzer, coupled to a scrambler placed at the spectrometer entrance. In this way either parallel or crossed polarized spectra were carried out depending on the alignment of the analyzer plate with respect to the polarizer one ($\overline{E}_s \| \overline{E}_i$ or $\overline{E}_s \perp \overline{E}_i$).

Several micro-Raman measurements were carried out under the same polarization condition from different regions of the micro-crystal under investigation, and the spectra showed a very good reproducibility. In particular, no detectable Raman scattering from crystalline phases other than the NASICON structure was observed on the analyzed LTP. Likewise, the presence of luminescent impurities was also ruled out by recording the luminescence spectra from several sample regions

under excitation at different wavelengths. In general, the as-recorded polarized spectra were superimposed to a very flat and structureless luminescence background. Moreover, no relevant mosaic spread (i.e. orientational misalignment of the micro-crystalline domains) in the individual small crystals was detected by this systematic inspection. Finally, the recorded spectra were processed to remove artefacts due to cosmic rays, while the luminescence background, due to its relatively low intensity, was not removed before starting the analysis of the experimental data.

## First-principles calculations

The vibrational properties of crystalline $LiTi_2(PO_4)_3$ have been simulated by first-principles calculations based on density functional theory in the generalized gradient approximation. The simulation will help us in the experimental symmetry assignment of the Raman vibrational modes. The CRYSTAL14 program package[55,56] was used in the present computational study. CRYSTAL is a periodic first-principles program which adopts a Gaussian-type basis set to describe the atomic orbitals. Further details on basis sets and computational parameters can be found at the CRYSTAL website.[57] In this specific study, all-electron basis sets have been used, with 61-1G contractions (two s and one p shell) for lithium atoms,[58] 86-411(d31)G contractions (one s, four sp and two d shell) for titanium,[59,60] 85-21d1G (one s, three sp, and one d shell) for phosphorus[61] and 6-31d1 (one s, two sp, and one d shell) for oxygen.[62] Pure density-functional theory calculations have been performed by using Perdew-Becke-Ernzerhof exchange and correlation functionals revised for solids.[63] The tolerances for Coulomb and exchange sums is controlled by five parameters, for which (7 7 7 7 14) values have been used. To guarantee a good convergence, self-consistent field convergence threshold on total energy of $10^{-9}$ Hartree has been employed in the geometry optimization and $10^{-10}$ Hartree in the frequency calculation. The integration of the Brillouin zone was conducted with a $6\times6\times6$ Monkhorst-Pack grid centered at the $\Gamma$-point.[64,65] The vibrational frequencies at the $\Gamma$-point were obtained within the harmonic approximation by diagonalizing the mass-weighted Hessian matrix, while the Raman and infrared intensities were calculated via the Coupled Perturbed Hartree-Fock/Kohn-Sham method.[66,67] More details on the computational as-

pects can be found in Refs.[68,69]

# Experimental results and discussion

## X-ray diffraction

The cell parameters and the atomic coordinates were determined from this single crystal X-ray diffraction study as well as the anisotropic thermal displacement parameters, and are listed in Tab. 1. Intensity statistics and systematic extinctions were in agreement with space group $R\bar{3}c$ (Fig. 1), which is the typical space group symmetry for the NASICON-type materials. The Li positions were determined from detailed inspection of residual electron density maps (Fig. 2). Structure solution with direct methods gave the Ti1 on 12*c*, P1 on 18*e* and the two oxygen atom positions O1 and O2, both on 36*f*, which agree very well with the atomic positional parameters previously published from neutron powder diffraction data.[33,70] The largest peak in the residual electron density map was located at position 0, 0, 0, corresponding to the 6*b* position. A portion of the unit cell using the refined atomic positions is shown in Figure 3. Adding Li in full occupation to this site in pure LTP decreases the $R_1$-values to 1.67 % and $wR_2$ = 4.49 %. Both values indicate the high quality of the structural refinement. With Li1 in 6*b* there are no additional evidences in the very flat difference electron density maps for Li on other possible sites in the NASICON-type structure (Fig. 2). The "largest" residual electron density peak is +0.34 e/Å$^3$ with a distance of 0.74 Å to P1. Bond lengths in LTP agree very well with literature data of Aatiq *et al.*,[33] but deviate to some extent from those of Bournar *et al.*[34] and Pinus *et al.*[18] The $PO_4$ tetrahedron is very regular, both in terms of angular and bond angle distortion; here the powder X-ray diffraction data exhibit a distinct more distorted environment, which - in the light of the present study - does not actually reflect the true $PO_4$ geometry in $LiTi_2(PO_4)_3$. The same is true for the $TiO_6$ octahedron, for which we find a regular geometry, while especially the data of Bournar *et al.*[34] exhibit much higher elongation and bond angle variance. Note that the Li atoms have large anisotropic thermal displacements in the crystallographic *ab* plane.

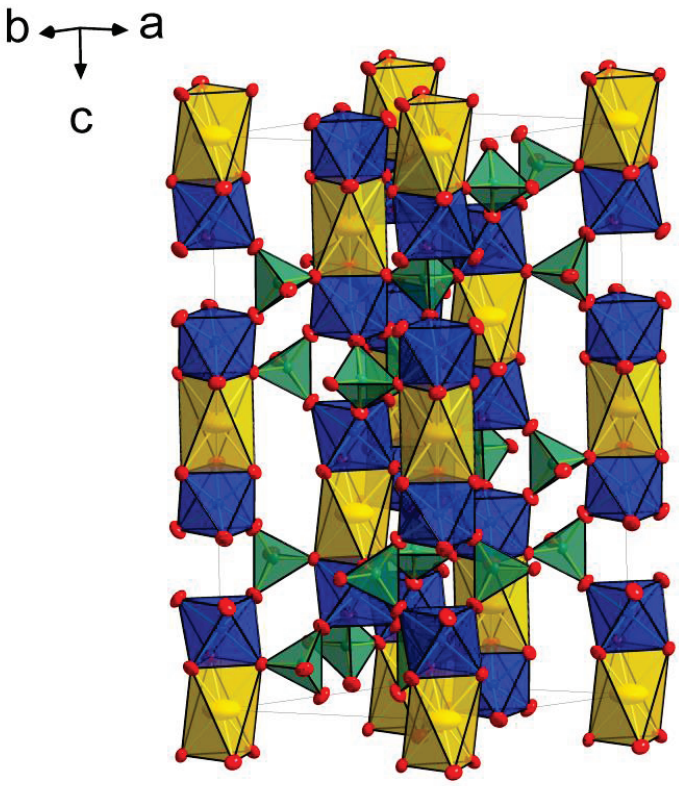


Figure 1: Unit cell (space group $R\bar{3}c$) of $LiTi_2(PO_4)_3$. Yellow elongated octahedra ($M_1$/6*b*) are occupied by $Li^+$, blue octahedra ($M_2$/12*c*) are occupied by $Ti^{4+}$, green tetrahedra are occupied by $P^{5+}$ (18*e*). $O^{2-}$ is located at the corners of the polyhedra (small red circles, two Wyckoff positions 36*f*).

Table 1: Crystal structure of $LiTi_2(PO_4)_3$ (Wyckoff positions and lattice parameters) and anisotropic thermal displacement parameters obtained from the single-crystal X-ray diffraction study at room temperature.

| | x | y | z | $U_{11}$ | $U_{22}$ | $U_{33}$ | $U_{23}$ | $U_{13}$ | $U_{12}$ | $U_{eq}$ |
|---|---|---|---|---|---|---|---|---|---|---|
| Li | 0.0000 | 0.0000 | 0.0000 | 0.066(4) | 0.066(4) | 0.018(4) | 0 | 0 | 0.033(2) | 0.050(3) |
| Ti | 0.0000 | 0.0000 | 0.14171(2) | 0.0059(2) | 0.0059(2) | 0.0056(2) | 0 | 0 | 0.0030(1) | 0.0058(1) |
| P | 0.29052(5) | 0.0000 | 0.2500 | 0.0053(2) | 0.0065(2) | 0.0070(2) | 0.0016(1) | 0.0008(1) | 0.0032(1) | 0.0061(2) |
| O1 | 0.1849(1) | 0.9957(1) | 0.19005(5) | 0.0115(5) | 0.0139(5) | 0.0130(5) | 0.0020(4) | -0.0038(2) | 0.0069(4) | 0.0126(2) |
| O2 | 0.1883(1) | 0.1640(1) | 0.08094(5) | 0.0076(4) | 0.0095(4) | 0.0098(5) | 0.0021(3) | 0.0012(3) | 0.0016(4) | 0.0101(2) |
| a=8.5179(5) Å | c=20.8584(12) Å | c/a=2.449 | | | | | | | | |

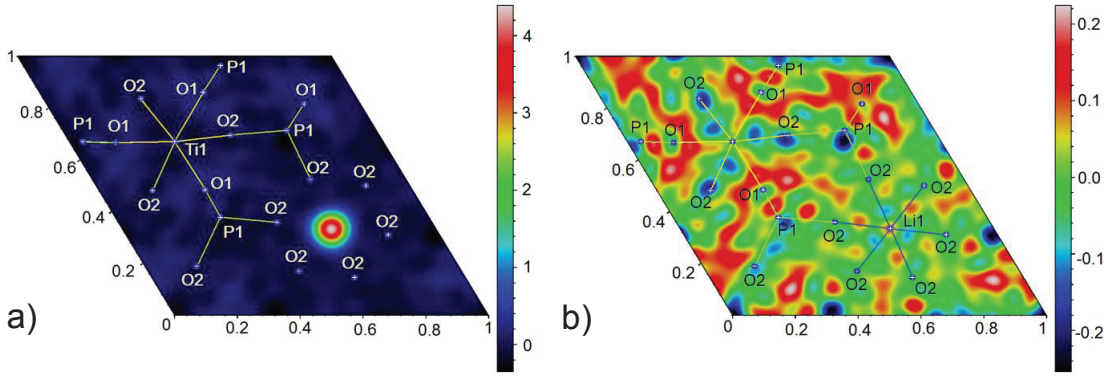


Figure 2: $F_{obs} - F_{cal}$ residual electron density maps in the x-y plane calculated for z=1/3. Positions of atoms and bonds are marked. In (a) the Li1 position is excluded from the refinement thus showing a clear and easy view to locate the residual electron density peak. In (b) Li1 is included and no interpretable residual electron density is left, note the very low residual electron densities of -0.2< $\rho$ <0.2 eÅ$^{-1}$.

## Polarized Raman spectra

As it is shown in Fig. 1, crystalline $LiTi_2(PO_4)_3$ consists of a three dimensional network of corner-sharing $TiO_6$ octahedra and $PO_4$ tetrahedra.[10] Within this structure $Li^+$ ions occupy interstitial sites, denoted as Li1, according to the XRD refinements above (see also Figure 3). Both Li and Ti possess octrahedral coordination with respect to the chemical bonding, the $PO_4$ tetrahedron consists of two types of oxygen atoms, one of them (O1) is also bound to one $Ti^{4+}$, whereas the second one (O2) is bound to one $Ti^{4+}$ and one $Li^+$.

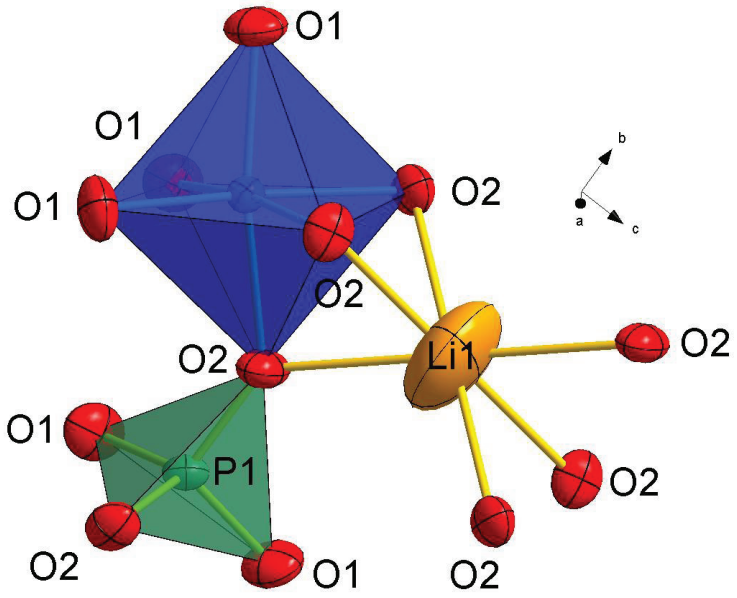


Figure 3: Part of the NASICON-type $LiTi_2(PO_4)_3$ crystal structure. Small circles denote titanium atoms octahedrally coordinated to oxygen atoms (medium ellipsoids). Big ellipsoids indicate lithium atoms in octahedral sites. Finally small ellipsoids indicate phosphorus atoms tetrahedrally coordinated to oxygen atoms.

Its vibrational dynamics is usually described in terms of internal and external modes, the first ones being related to vibrational modes, i.e. stretching and bending vibrations of $(PO_4)^{3-}$ anions, while the second ones include both the translational modes of the $Li^+$, $Ti^{4+}$ and $(PO_4)^{3-}$ ions as well as the $(PO_4)^{3-}$ librations.[35] A different approach describes the vibrational dynamics of the crystal structure in terms of vibrational modes, regardless to their internal or external character. Their symmetry can be derived directly from the crystallographic elementary cell, while their vibrational frequency can be obtained by means of first-principles calculations.[55,66] This approach allows to determine all the vibrational modes of the crystal, and to predict if they are Raman active, IR active or silent, together with their symmetry.

NASICON-type $LiTi_2(PO_4)_3$ crystallizes in the rhombohedral space group $R\bar{3}c$ (point group $D_{3d}$, in Schoenfliess notation), with six formula units per unit cell. Among its 108 degrees of freedom, originating from the 36 atoms contained in its primitive cell, only 25 are expected to be Raman active, i.e. 8 $A_{1g}$ + 17 $E_g$, while 27 are infrared active, i.e., 18 $E_u$ + 9 $A_{2u}$, and 17 are silent modes, i.e., 8 $A_{2g}$ + 9 $A_{1u}$. Due to the quite high number of modes and to the limited number

of irreducible representations of the rhombohedral $R\bar{3}c$ space group, the symmetry assignment of an observed Raman peak at a given wavenumber to a definite type of vibration is, in some instances, impossible. However, a careful selection of the symmetry of the vibrational modes can be obtained through a proper polarization analysis of the Raman scattering from the crystal. In fact, according to Loudon[71] in correspondence to each Raman-active mode of NASICON-type rhombohedral orthophosphates, there is a scattering tensor $\alpha$ having a distinctive symmetry:

$$\alpha(A_{1g}) = \begin{pmatrix} a & 0 & 0 \\ 0 & a & 0 \\ 0 & 0 & b \end{pmatrix} \tag{1}$$

$$\alpha(E_g) = \begin{pmatrix} c & 0 & 0 \\ 0 & -c & d \\ 0 & d & 0 \end{pmatrix} \tag{2}$$

$$\alpha(E_g) = \begin{pmatrix} 0 & -c & -d \\ -c & 0 & 0 \\ -d & 0 & 0 \end{pmatrix} \tag{3}$$

To examine experimentally a given component $\alpha_{ij}$ the scattering experiment has to be arranged in such a way that the incident light is polarized in the "$i$" direction while only the scattered light with "$j$" polarization is observed. In order to perform such a polarization analysis of the highly anisotropic NASICON structure, the first step is the perfect alignment of the crystallographic $c$-axis along the direction of the electric field of the laser beam impinging on the sample surface. In this way it is possible to discriminate the Raman modes with symmetry $A_{1g}$ (total symmetric modes) from those with $E_g$ symmetry by simply switching from the parallel to the crossed polarization setting. After having determined the crystallographic $c$-axis direction and performed the above polarization analyses, the next step consists of a proper rotation of the crystal to align the c-axis with the propagation direction of the incident laser beam. In fact, this configuration allows for the

excitation of all the Raman active modes associated with atomic motions in the basal (a,b) plane of the LTP crystal, regardless to their $A_{1g}$ or $E_g$ symmetry character. Of course, also in this case, a more exhaustive and accurate symmetry assignment of the "in-plane" modes can be then achieved by the polarization analysis carried out in both parallel and crossed settings. This step-by-step experimental approach was successfully adopted by us to select and assign the symmetry of all the expected Raman modes.

Figure 4 shows the full set of Raman spectra of an LTP micro-crystal recorded in backscattering geometry for the different polarization configurations. All spectra were recorded from the same micro-crystal when its crystallographic *c*-axis was aligned along (spectra in panels(a) and (b)) or perpendicular (spectra in panels (c) and (d)) to the electric field direction of the laser beam. The spectra (a), (b) and (d) were recorded during the same acquisition time of 150 s, while the acquisition time for spectrum (c) was 300 s. Nevertheless, all these spectra turn out to be superimposed over a weak, very flat and structureless background, which indicates the absence of luminescent impurities inside the crystal. Both the spectra (a) and (b) are characterized by a stronger scattering intensity, compared with the spectra (c) and (d), as it can be inferred by the respective full scales. This finding reveals an overall stronger Raman intensity related to the vibrational modes involving ion displacements out of rather than within the basal plane of LPT.

In detail, Figure 4(a) shows the spectrum carried out in parallel polarization, with both the electric field of the incident laser beam and of the scattered radiation aligned along the crystallographic *c*-axis of the crystal. Hence only the (z,z) component of the Raman tensor is selected, which, according to eq. 1, allows for the observation of the pure $A_{1g}$ spectrum. In fact, in this spectrum seven distinct Raman modes of $A_{1g}$ symmetry are clearly identified, peaked at about 178, 312.5, 432.5, 450.5, 610, 1018.5 and 1095 $cm^{-1}$, even if the intensity of the two modes peaked at about 450.5 and 610 $cm^{-1}$ are extremely weak, so that a proper spectral magnification was mandatory for their unambiguous identification. Besides these 7 $A_{1g}$ modes, some small peaks (labeled by a *) also occur: they are due to the spill-over of forbidden $E_g$ modes, as it can be inferred by looking at the spectrum reported in the panel (b) of the same figure.

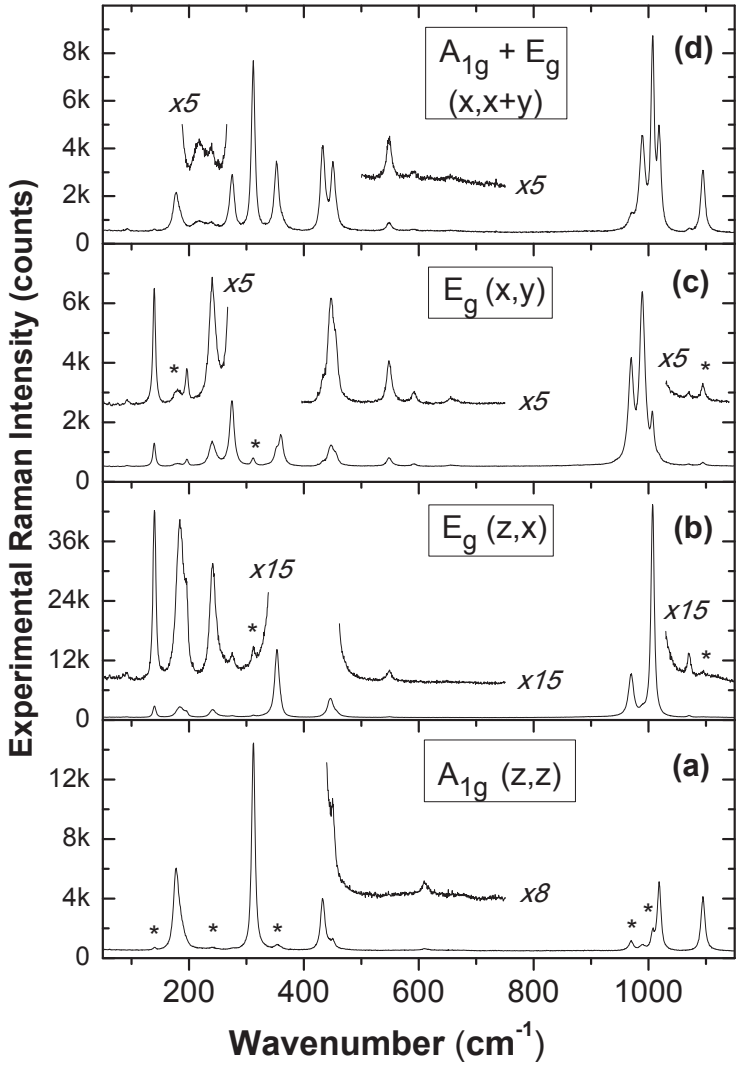


Figure 4: Polarized micro-Raman spectra of an LTP micro-crystal carried out in backscattering geometry under excitation of the 514.5 nm laser line after preliminary alignment of the crystallographic *c*-axis along (spectra (a) and (b)) and perpendicular to (spectra (c) and (d)) the direction of the electric field of the incident laser radiation. (a) Spectrum recorded in parallel polarization, showing the $A_{1g}$ (z,z) symmetry modes, where z coincides with the crystallographic c-axis; (b) spectrum observed in crossed polarization, displaying the $E_g$ (z,x) symmetry modes, where x and y are orthogonal axes of the basal (a,b) plane of the LTP crystal; (c) spectrum recorded in crossed polarization, showing the "in-plane" modes of $E_g$ (x,y) symmetry, with x and y orthogonal axes of the basal (a,b) plane of the LTP crystal; (d) spectrum observed in parallel polarization, showing the "in-plane" modes of either $A_{1g}$ (x,x) or $E_g$ (x,y) symmetry. Note the full scale values of Raman intensity adopted to properly display the spectral intensity related to the different polarization. Parts of the spectra are properly magnified in order to better visualize the Raman peaks with very weak intensity. Finally, the stars (*) just above individual Raman modes label the main spills of forbidden modes.

Figure 4(b) displays the spectrum observed in crossed polarization with the electric field of the scattered radiation perpendicular to the crystallographic *c*-axis of the crystal. This scattering configuration allows for the selection of the (z,x) or (z,y) component of the Raman tensor, where x and y are orthogonal axes of the basal (a,b) plane of the LTP crystal, and will be hereafter referred by the notation (z,x). According to eqs. 2 and 3, it allows for the observation of the $E_g$ spectrum associated to vibrational modes having a tensor component perpendicular to the basal plane. This spectrum consists of Raman peaks either very strong, characterized by an extremely high signal-to-noise ratio, or very weak, so that a proper spectral magnification is required for their unambiguous identification. It clearly displays twelve different Raman modes peaked at about 92, 139.5, 185, 196.5, 240.5, 274.5, 353, 446.5, 546.5, 969.5, 1007 and 1071 $cm^{-1}$. This count of Raman modes does not takes into account the minor spectral component (labeled by a *) resulting from the spill-over of the strongest $A_{1g}$ mode observed in Figure 4(a).

However, in order to get both a more exhaustive selection and an accurate symmetry assignment of the Raman modes, the polarization analysis should be extended also to Raman scattering related to vibrational modes involving ion displacements within the basal (a,b) plane, i.e. the so-called "in-plane" modes of the LTP crystal. In fact, when the propagation direction of the laser beam matches the *c*-axis of the crystal, the observed polarized Raman spectra show much more spectral details than in the case of the previous alignment, in spite of the overall minor spectral intensity.

Panels (c) and (d) of Figure 4 show the typical full Raman spectra having the *c*-axis of the crystal aligned along the propagation direction of the incident laser beam for the two (parallel and crossed) polarization settings. Due to the overall weakness of Raman scattering from in-plane modes of the LTP crystal, a proper magnification of some spectral region was adopted in order to ensure a clearer observation of the weakest Raman modes, together with their unambiguous assignment in symmetry.

The spectrum of Figure 4(c), carried out in crossed polarization shows the "in-plane" modes of $E_g$ (x,y) symmetry, where x and y are orthogonal axes of the basal (a,b) plane of the LTP crystal. It displays a number of $E_g$ symmetry Raman modes higher than that of Figure 4(b). In fact, besides

the twelve modes observed in the $E_g$ (z,x) spectrum, it clearly shows four additional modes: the first one occurring at about 360 $cm^{-1}$, which surpasses in intensity and almost completely overlaps the peak at 253 $cm^{-1}$ previously identified by analyzing the spectrum of Figure 4(b), where it turns out clearly visible. The second mode appears as the very weak peak at 591.5 $cm^{-1}$, while the third one is the even weaker peak at 656.5 $cm^{-1}$. Finally the fourth one is clearly associated to the strongest peak occurring at 989 $cm^{-1}$. Therefore, the total number of the detected $E_g$ modes turns out to be sixteen, one less than the expected number for NASICON structure on the basis of group theory.

In the aim to search for the two missing modes, one $A_{1g}$ and one $E_g$, the parallel polarization setting was exploited, since it allows for simultaneous selection of both (x,x) or (x,y) components of the Raman tensor, related to the "in-plane" modes of the LTP crystal. The related Raman spectrum will be hereafter referred by the notation (x,x+y). In fact, the spectrum, carried out in this scattering configuration, according to eqs. 1 and 2, is expected to display both the $A_{1g}$ and $E_g$ symmetry modes whose eigenvectors belong to the basal plane of the LTP crystal. In fact, the observed spectrum, reported in Figure 4(d), is very rich of spectral features showing nearly all (i.e. 24 of 25) of the expected Raman active modes of this crystal. In particular, it shows the presence of the missing $A_{1g}$ mode at $\sim$218 $cm^{-1}$, clearly visible in the magnified part of the spectrum and also confirmed by our first-principles calculations (see below). By the way, it should be stressed that this mode was not detected in the pure $A_{1g}$ (z,z) spectrum (a) even not after the magnification of it, due to its negligible intensity in the (z,z) configurational setting. Unfortunately no evidence of the missing $E_g$ can be inferred from the spectrum (d) carried out in parallel polarization. In conclusion, the step-by-step approach, consisting of the serial analysis of the polarized micro-Raman spectra revealed unambiguously both wavenumber and symmetry of twenty-four distinct modes of the twenty-five expected on the basis of group theory. In particular, all the height $A_{1g}$ modes were clearly contrasted and definitely identified either in wavenumber or in symmetry, while sixteen $E_g$ Raman modes were identified instead of the seventeen expected ones.

The last chance to find the missing $E_g$ relies on the adoption of a different approach based

on the direct comparative analysis of the spectral profiles observed in the different polarization configurations. The search of the missing $E_g$ mode based on such approach was systematically carried out by analyzing in detail the spectral profiles in correspondence of different energy regions. Special attention was devoted to profile analysis of the spectral features occurring in the region between 400 and 500 $cm^{-1}$ were an important overlap of different nearly degenerate Raman modes occurs as already evidenced in the description of Figure 4(b). Figure 5 displays the plots in the same full scale of the experimental micro-Raman spectra of LTP recorded in the spectral region between 420 and 470 $cm^{-1}$ in the four different polarization configurations accessible in the backscattering geometry. Regardless to the symmetry character, in this spectral region four different Raman modes of LTP crystal can be clearly identified. The three modes peaking at about 433, 446.5 and 450.5 $cm^{-1}$ were already clearly detected in the description of the single spectra of Figure 4 (a), (b) and (d), respectively, and, thus, unambiguously assigned in symmetry. Moreover, the direct comparison of the spectra reveals the fourth Raman mode, peaking at about 457 $cm^{-1}$, which, in spite of very weak intensity of its components, is definitely identified as an $E_g$ mode. It is the missing mode that completes the series of twenty five Raman modes expected for the NASICON-type LTP crystal according to group theory. Also this latest mode assignment is fully confirmed by our first-principles calculations, as reported below.

# Computational results

As first step, a full geometry optimization was carried out and returned the cell parameters and the atomic coordinates listed in Tab. 2. The calculated lattice parameters a=b=8.5418 Å, c=20.5219 Å and c/a=2.403, differ from the experimental data reported in Tab. 1 by about 0.3, 1.6, and 1.9 %, respectively. Also the atomic positions in the conventional cell are fully consistent with that listed in Tab. 1, thus further corroborating the results obtained from the refinement of the X-ray diffraction data. These structural parameters have been used in the frequency calculations reported below.

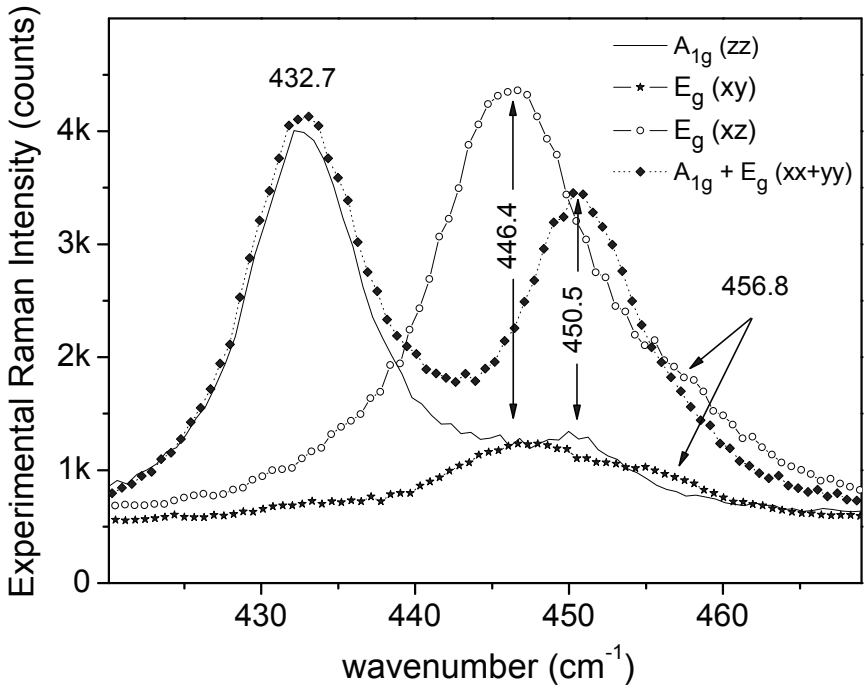


Figure 5: Experimental micro-Raman spectra of LTP ç observed in the spectral region between 420 and 470 $cm^{-1}$ and carried out in backscattering geometry for the 4 different polarization configurations, quoted in the inset. The spectra are plotted in the same full scale in order to allow for a clear and unambiguous identification of each single Raman mode and of the related symmetry. Four different Raman modes of LTP crystal can be clearly identified. The wavenumber value of each Raman component is indicated at its maximum intensity, as derived by a fitting procedure based on Gaussian curves. The symmetry character of each Raman mode can be straightforwardly assessed by considering the intensity of its spectral components observed in the different polarization configurations. Therefore, according to this procedure, the Raman mode at about 457 $cm^{-1}$ is definitely identified as an $E_g$ mode despite of very weak intensity of its components.

The calculated frequencies and intensities of the Raman active modes of $LiTi_2(PO_4)_3$, compared with the experimental data obtained in the present study, are listed in Tab. 3. Firstly, we observe that our identification of the two missing modes, one $A_{1g}$ and one $E_g$ respectively assigned at about 218 and 457 $cm^{-1}$, is fully supported by the present computational study, which predicts the vibrational frequency of these two modes at 225.5 and 448.9 $cm^{-1}$, respectively.

The overall comparison between calculated ($\nu^{cal}$) and experimental ($\nu^{exp}$) Raman frequencies have been determined by three parameters defined as follows:

$$\overline{|\Delta|} = \frac{1}{N}\sum_{i=1}^{N}|\nu_i^{cal} - \nu_i^{exp}| \tag{4}$$

$$\overline{|\Delta_r|}\% = \frac{100}{N}\sum_{i=1}^{N}\left|\frac{\nu_i^{cal} - \nu_i^{exp}}{\nu_i^{exp}}\right|$$

$$|\Delta_{max}| = \max(|\nu_i^{cal} - \nu_i^{exp}|)$$

where $i = 1, ..., N$ indicates the 25 Raman modes listed in Table 3, $|\overline{\Delta}|$ is the average of the absolute difference, $\overline{|\Delta_r|}\%$ the average of the absolute "relative" differences (in percentage), and $|\Delta_{max}|$ is the maximum difference. The three indices, listed at the end of Table 3, show the excellent agreement between our calculations and experimental data. This definitely corroborates our experimental findings and symmetry assignment of the Raman modes.

Table 2: Crystal structure of $LiTi_2(PO_4)_3$ (Wyckoff positions and lattice parameters) obtained from the present first-principles calculations. The agreement with the crystal structure determined from X-ray single-crystal diffraction data (see Tab. 1) is very good.

| | x | y | z |
|---|---|---|---|
| Li | 0.0000 | 0.0000 | 0.0000 |
| Ti | 0.0000 | 0.0000 | 0.1395 |
| P | 0.2921 | 0.0000 | 0.2500 |
| O1 | 0.1902 | 0.9951 | 0.1886 |
| O2 | 0.1846 | 0.1639 | 0.0768 |
| a=8.5418 Å | c=20.5219 Å | c/a=2.403 | |

In Table 4, we also report the calculated frequencies for all the other vibrational modes at the center of the Brillouin zone, i.e., the infrared active and silent modes, including the calculated infrared intensity (quoted within the square brackets). In the literature, there is not a well-defined assignment of the infrared modes of LTP (and of similar NASICON-type compounds), although some experimental works have been published on this issue.[43,44,72] This is due to the broad infrared bands observed in LTP which does not allow the discrimination of the large number of infrared modes involved. However, the calculated data reported in Tab. 4 agree with the main features of the experimental infrared spectra,[43,44,72] so providing additional information on the lattice dynamics of LTP. For example, according to Tab. 4, we can see that the intense band experimentally observed between ~950-1050 $cm^{-1}$ is the result of the presence of four intense infrared modes, i.e., $3E_u + 1A_{2u}$ symmetry modes; or the peak of medium intensity at ~1223 $cm^{-1}$ corresponds to the $A_{2u}(9)$ vibrational mode calculated at 1218 $cm^{-1}$. Again, the three infrared bands observed at about 575, 585 and 644 $cm^{-1}$ correspond to the infrared modes of medium intensity calculated at ~562, 573 and 628 $cm^{-1}$, respectively. More confusing is the situation between 200-500 $cm^{-1}$ due to the discrepancies between experimental data. However, from Tab. 4, the intense bands observed in this wavenumber range by Refs.[43,44,72] are related to the six intense $3E_u + 3A_{2u}$ symmetry modes predicted at about 256, 286, 309, 311, 336 and 355 $cm^{-1}$.

Before concluding, we point out that from the calculated atomic eigenvectors listed in the Supporting Information, it can be observed that Li atoms are frozen in all the Raman active vibrational modes ($E_g$ and $A_{1g}$ symmetry) and in the $A_{2g}$ silent modes. In contrast, Li atoms vibrate along the c-axis direction in the $A_{2u}$ infrared active modes and in the $A_{1u}$ silent modes, in-phase in the first case, in phase-opposition in the second one. Finally, in the $E_u$ infrared active modes, Li atoms vibrate on the a-b crystallographic plane. In general, this should be taken into consideration in the study of the correlation between vibrational properties and Li ions conduction in Nasicon-type materials.

Table 3: Experimental and calculated Raman frequencies of $LiTi_2(PO_4)_3$ (in $cm^{-1}$) as determined in this study. The calculated Raman intensity (in % of the strongest mode) is reported in the square brackets and it was computed for the excitation wavelength of 514.5 nm. The three indices $|\overline{\Delta}|$, $|\overline{\Delta}_r|\%$ and $|\Delta_{max}|$ (see text) are reported at the end of the table.

| Raman modes | Experimental | Calculated |
|---|---|---|
| $E_g(1)$ | 92.0 | 88.4 [0.06] |
| $E_g(2)$ | 139.6 | 130.5 [0.79] |
| $A_{1g}(1)$ | 177.8 | 177.9 [1.11] |
| $E_g(3)$ | 185.0 | 192.2 [1.29] |
| $E_g(4)$ | 196.4 | 196.5 [0.49] |
| $A_{1g}(2)$ | 218.5 | 225.5 [0.13] |
| $E_g(5)$ | 240.5 | 237.6 [2.79] |
| $E_g(6)$ | 274.5 | 271.9 [2.50] |
| $A_{1g}(3)$ | 312.4 | 293.6 [10.74] |
| $E_g(7)$ | 353.1 | 343.8 [3.92] |
| $E_g(8)$ | 360.1 | 358.2 [10.11] |
| $A_{1g}(4)$ | 432.7 | 416.6 [4.30] |
| $E_g(9)$ | 446.4 | 421.3 [7.01] |
| $A_{1g}(5)$ | 450.5 | 436.2 [7.16] |
| $E_g(10)$ | 456.8 | 448.9 [1.63] |
| $E_g(11)$ | 546.5 | 528.0 [0.68] |
| $E_g(12)$ | 591.4 | 576.4 [0.61] |
| $A_{1g}(6)$ | 610.3 | 599.1 [0.14] |
| $E_g(13)$ | 656.3 | 645.4 [2.19] |
| $E_g(14)$ | 969.5 | 992.8 [2.02] |
| $E_g(15)$ | 989.1 | 1003.0 [42.24] |
| $E_g(16)$ | 1007.3 | 1017.8 [100.0] |
| $A_{1g}(7)$ | 1018.6 | 1035.6 [43.36] |
| $E_g(17)$ | 1071.0 | 1065.0 [2.16] |
| $A_{1g}(8)$ | 1095.0 | 1081.9 [13.53] |
| $\|\overline{\Delta}\|$ | 10.6 | |
| $\|\overline{\Delta}_r\|\%$ | 2.4 % | |
| $\|\Delta_{max}\|$ | 25.1 | |

Table 4: Infrared and silent vibrational frequencies of $LiTi_2(PO_4)_3$ (in $cm^{-1}$) as calculated in this study. The calculated IR intensity (in % of the strongest mode) is reported in the square brackets.

| Infrared modes | Calculated |
|---|---|
| $E_u(1)$ | 86.2 [0.43] |
| $E_u(2)$ | 100.5 [0.00] |
| $A_{2u}(1)$ | 109.5 [0.65] |
| $E_u(3)$ | 123.8 [2.04] |
| $A_{2u}(2)$ | 174.8 [5.32] |
| $E_u(4)$ | 184.8 [6.09] |
| $E_u(5)$ | 209.2 [0.76] |
| $A_{2u}(3)$ | 256.4 [29.77] |
| $E_u(6)$ | 270.6 [1.97] |
| $E_u(7)$ | 286.4 [10.71] |
| $A_{2u}(4)$ | 309.2 [17.88] |
| $E_u(8)$ | 311.3 [43.47] |
| $E_u(9)$ | 336.4 [100.0] |
| $E_u(10)$ | 347.2 [3.15] |
| $A_{2u}(5)$ | 355.3 [22.60] |
| $E_u(11)$ | 420.1 [2.06] |
| $E_u(12)$ | 527.9 [0.00] |
| $A_{2u}(6)$ | 562.3 [9.70] |
| $E_u(13)$ | 573.0 [8.61] |
| $A_{2u}(7)$ | 628.4 [10.83] |
| $E_u(14)$ | 671.4 [1.67] |
| $E_u(15)$ | 989.2 [97.61] |
| $E_u(16)$ | 1000.4 [76.55] |
| $A_{2u}(8)$ | 1016.7 [88.11] |
| $E_u(17)$ | 1022.6 [90.96] |
| $E_u(18)$ | 1058.9 [8.53] |
| $A_{2u}(9)$ | 1218.4 [15.34] |
| Silent modes | |
| $A_{2g}(1)$ | 45.8 |
| $A_{1u}(1)$ | 145.6 |
| $A_{2g}(2)$ | 169.6 |
| $A_{1u}(2)$ | 233.3 |
| $A_{2g}(3)$ | 238.8 |
| $A_{1u}(3)$ | 275.8 |
| $A_{2g}(4)$ | 289.1 |
| $A_{2g}(5)$ | 377.6 |
| $A_{1u}(4)$ | 384.3 |
| $A_{1u}(5)$ | 432.8 |
| $A_{1u}(6)$ | 512.7 |
| $A_{2g}(6)$ | 540.9 |
| $A_{1u}(7)$ | 554.8 |
| $A_{2g}(7)$ | 696.3 |
| $A_{2g}(8)$ | 1056.8 |
| $A_{1u}(8)$ | 1068.7 |
| $A_{2g}(9)$ | 1220.7 |
| $A_{1u}(9)$ | 1226.9 |

# Conclusions

In this study both the crystal structure and the vibrational dynamics of NASICON-type $LiTi_2(PO_4)_3$ crystal have been carried out by single crystal X-ray diffraction and an integrated vibrational dynamics study of LTP single crystals, consisting of polarized Raman scattering measurements and first-principles calculations. In particular, the structural parameters were carefully determined, like cell parameters, atomic positions and anisotropic thermal displacement parameters. Moreover, all the allowed Raman modes of LTP have been unambiguously detected and identified in terms of their frequency and symmetry. Our experimental findings resulted in excellent agreement with the results of first-principles calculations, which also provide additional insights into the infrared and silent vibrational modes. These structural and dynamical information on LTP, reference compound for NASICON-type materials, would help in outlining a thorough description of ion transport and related properties of NASICON-type solid electrolytes.

## References


(1) Bachman, J.C.; Muy, S.; Grimaud, A.; Chang, H.-H.; Pour, N.; Lux, S.F.; Paschos, O.; Maglia, F.; Lupart, S.; Lamp, P. et al. *Chem. Rev.* **2016**, *116*, 140.

(2) Knauth, P. *Solid State Ionics* **2009**, *180*, 911.

(3) Thangadurai, V.; Shukla, A. K.; Gopalakrishnan, J. *J. Mater. Chem.* **1999**, *9*, 739.

(4) Sebastian, L.; Gopalakrishnan, J. *J. Mater. Chem.* **2003**, *13*, 433.

(5) Xu, X.; Wen, Z.; Wu, X.; Yang, X.; Gu, Z. *J. Am. Ceram. Soc.* **2007**, *90*, 2802.

(6) Feng, J. K.; Xia, H.; Lai, M.O.; Lu, L. *J. Phys. Chem. C* **2009**, *113*, 20514.

(7) Shimonishi, Y.; Zhang, T.; Johnson, P.; Imanishi, N.; Hirano, A.; Takeda, Y.; Yamamoto, O.; Sammes, N. *J. Power Sources* **2010**, *195*, 6187.

(8) Anantharamulu, N.; Koteswara Rao, K.; Rambabu, G.; Vijaya Kumar, B.; Velchuri Radha; Vithal, M. *J. Mater. Sci.* **2011**, *46*, 2821.

(9) Hartmann, P.; Leichtweiss, T.; Busche, M. R.; Schneider, M.; Reich, M.; Sann, J.; Adelhelm, P.; Janek, J. *J. Phys. Chem. C* **2013**, *117*, 21064.

(10) Delmas, C.; Nadiri, A.; Soubeyroux, J. L. *Solid State Ionics* **1998**, *28-30*, 419.

(11) Takada, K.; Tansho, M.; Yanase, I.; Inada, T.; Kajiyama, A.; Kouguchi, M.; Kondo, S.; Watanabe, M. *Solid State Ionics* **2001**, *139*, 241.

(12) Wang, G. X.; Bradhurst, D. H.; Dou, S. X.; Liu, H. K. *J. Power Sources* **2003**, *124*, 231.

(13) Nuspl, G.; Takeuchi, T.; Weiß, A.; Kageyama, H.; Yoshizawa, K.; Yamabe, T. *J. Appl. Phys.* **1999**, *86*, 5484.

(14) Luo, J. Y.; Chen, L. J.; Zhao, Y. J.; He P.; Xia, Y. Y. *J. Power Sources* **2009**, *194*, 1075.

(15) Paris, M. A.; Martínez-Juárez, A.; Rojo, J. M.; Sanz, J. *J. Phys.: Cond. Matter* **1996**, *8*, 5355.

(16) Capsoni, D.; Bini, M.; Ferrari, S.; Mustarelli, P.; Massarotti, V.; Mozzati, M. C.; Spinella, A. *J. Phys. Chem. C* **2014**, *114*, 13872.

(17) Pinus, I. Y.; Shaikhlislamova, A. R.; Stenina, I. A.; Zhuravlev, N. A.; Yaroslavtsev, N. A. *Inorg. Mater.* **2009**, *45*, 1370.

(18) Pinus, I. Y.; Khoroshilov, A. V.; Gavrichev, K. S.; Tarasov, V. P.; Yaroslavtsev, A. B. *Solid State Ionics* **2012**, *212*, 112.

(19) Chandran, C. V.; Pristat, S.; Witt, E.; Tietz, F.; Heitjans, P. *J. Phys. Chem. C* **2016**, *120*, 8436.

(20) Li, S.-C.; Lin, Z.-X. *Solid State Ionics* **1983**, *9-10*, 835.

(21) Lin, Z.-X.; Yu, H.-J.; Li, S.-C.; Tian, S.-B. *Solid State Ionics* **1986**, *18-19*, 549.

(22) Subramanian, M. A.; Subramanian, R.; Clearfield, A. *Solid State Ionics* **1986**, *18-19*, 562.

(23) Martínez-Juárez, A.; Pecharromán, C.; Iglesias, J. E.; Rojo, J. M. *J. Phys. Chem. B* **1998**, *102*, 372.

(24) Kazakevičius, E.; Šalkus, T.; Dindune, A.; Kanepe, Z.; Ronis, J.; Kežionis, A.; Kazlauskiene, V.; Miškinis, J.; Selskiene, A.; Selskis, A. *Solid State Ionics* **2008**, *179*, 51.

(25) Aono, H.; Sugimoto, E.; Sadaoka, Y.; Imanaka, N.; Adachi, G.-Y. *J. Electrochem. Soc.* **1989**, *136*, 590.

(26) Aono, H.; Sugimoto, E., Sadaoka, Y.; Imanaka, N.; Adachi, G. *J. Electrochem. Soc.* **1990**, *137*, 1023.

(27) Kobayashi, Y.; Tabuchi, M.; Nakamura, O. *J. Power Sources* **1997**, *68*, 407.

(28) Saito, Y.; Ado, K.; Asai, T.; Kageyama, H.; Nakamura, O. *J. Mater. Sci. Lett.* **1992**, *11*, 888.

(29) Ma, Q.; Xu, Q.; Tsai, C.-L.; Tietz, F.; Guillon, O. *J. Am. Ceram. Soc.* **2016**, *99*, 410.

(30) Losilla, E. R.; Aranda, M. A. G.; Bruque, S. Chem. Mater. **1998**, *10*, 665-673.

(31) Kreuer, K. -D.; Kohler, H.; Maier, J. in: *High Conductivity Ionic Conductors: Recent Trends and Application*, ed.: T. Takahashi, World Scientific Publishing Co., Singapore, **1989**, 242-279.

(32) Tran Qui, D.; Hamdoune, S.; Sobeyroux, J. L.; Prince, E. *J. Solid State Chem.* **1988**, *72*, 309.

(33) Aatiq, A.; Ménétrier, M.; Croguennec, L.; Suard, E.; Delmas, C. *J. Mater. Chem.* **2002**, *12*, 2971.

(34) Bounar, N.; Benabbas, A.; Bouremmad, F.; Ropa, P.; Carru, J.-C. *Physica B* **2012**, *407*, 403.

(35) Tarte, P.; Rulmont, A.; Merckaert-Ansay, C. *Spectroch. Acta - Part A: Molecular Spectr.* **1986**, *42*, 1009.

(36) Barj, M. *J. Solid State Chem.* **1992**, *100*, 141.

(37) Barj, M. *Solid State Ionics* **1983**, *9-10*, 845.

(38) Kravchenko, V. V.; Michailov, V. I.; Sigaryov, S. E. *Solid State Ionics* **1992**, *50*, 19.

(39) Butt, G.; Sammes, N.; Tompsett, G.; Smirnova, A.; Yamamoto, O. *J. Power Sources* **2004**, *134*, 72.

(40) Aatiq, A.; Tigha, M. R.; Benmokhtar, S. *J. Mater. Sci.* **2012**, *47*, 1354.

(41) Francisco, B. E.; Stoldt, C. R.; M'Peko, J. C. *Chem. Mater.* **2014**, *26*, 4741.

(42) Francisco, B. E.; Stoldt, C. R.; M'Peko, J. C. *J. Phys. Chem. C* **2015**, *119*, 16432.

(43) Pikl, R.; de Waal, D.; Aatiq, A.; El Jazouli, A. *Mater. Res. Bull.* **1998**, *33*, 955.

(44) Burba, C. M.; Frech, R. *Solid State Ionics* **2006**, *177*, 1489.

(45) Venkateswara Rao, A.; Veeraiah, V.; Prasada Rao, A. V.; Kishore Babu, B.; Brahmayya, M. *Res. Chem. Intermed.* **2015**, *41*, 4327.

(46) Yue, Y.; Pang, W. *Mater. Res. Bull.* **1990**, *25*, 841.

(47) Rettenwander, D.; Welzl, A.; Pristat, S.; Tietz, F.; Taibl, S.; Redhammer, G. J.; Fleig, J. *J. Chem. Mater. A* **2016**, *4*, 1506.

(48) APEX2, SAINT and SADABS. Bruker AXS Inc., Madison, Wisconsin, USA.

(49) Sheldrick, G. M. *Acta Cryst.* **2008**, *A65*, 112.

(50) Farrugia, L. J. *J. Appl. Cryst.* **2012**, *45*, 849.

(51) Redhammer, G. J.; Rettenwander, D.; Pristat, S.; Dashjav, E.; Kumar, C. M. N.; Topa, D.; Tietz, F. *Solid State Sci.* **2016**, *60*, 99.

(52) Giarola, M.; Sanson, A.; Monti, F.; Mariotto, G.; Bettinelli, M.; Speghini, A.; Salviulo, G. *Phys. Rev. B* **2010**, *81*, 174305.

(53) Giarola, M.; Sanson, A.; Rahman, A.; Mariotto, G.; Bettinelli, M.; Speghini, A.; Cazzanelli, E. *Phys. Rev. B* **2011**, *83*, 224302.

(54) Damen, T. C.; Porto, S. P. S.; Tell, B. *Phys. Rev.* **1966**, *142*, 570.

(55) Dovesi, R.; Orlando, R.; Erba, A.; Zicovich-Wilson, C. M.; Civalleri, B.; Casassa, S.; Maschio, L.; Ferrabone, M.; De La Pierre, M.; D'Arco, Ph.; et al. *Int. J. Quantum Chem.* **2014**, *114*, 1287.

(56) Dovesi, R.; Saunders, V. R.; Roetti, C.; Orlando, R.; Zicovich-Wilson, C. M.; Pascale, F.; Civalleri, B.; Doll, K.; Harrison, N. M.; Bush, I. J.; et al. *CRYSTAL14 User's Manual*, Università di Torino, Torino, 2014.

(57) http://www.crystal.unito.it/index.php

(58) Dovesi, R.; Ermondi, E.; Ferrero, E.; Pisani, C.; Roetti, C. *Phys. Rev. B* **1983**, *29*, 3591.

(59) Bredow, T.; Heitjans, P.; Wilkening, M. *Phys. Rev. B* **2004**, *70*, 115111.

(60) Corà, F. *Mol. Phys.* **2005**, *103*, 2483.

(61) Zicovich-Wilson, C. M.; Bert, A.; Roetti, C.; Dovesi, R.; Saunders, V. R. *J. Chem. Phys.* **2002**, *116*, 1120.

(62) Corno, M.; Busco, C.; Civalleri, B.; Ugliengo, P.; *Phys. Chem. Chem. Phys.* **2006**, *8*, 2464.

(63) Perdew, J. P.; Ruzsinszky, A.; Csonka, G. I.; Vydrov, O. A.; Scuseria, G. E.; Constantin, L. A.; Zhou, X.; Burke, K. *Phys. Rev. Lett.* **2008**, *100*, 136406.

(64) Monkhorst, H.; Pack, J. *Phys. Rev. B* **1976**, *13*, 5188.

(65) Pisani, C.; Dovesi, R.; Roetti, C. *Hartree-Fock ab initio Treatment of Crystalline Systems*, Lecture Notes in Chemistry, Vol. 48 (Springer Verlag, Heidelberg, 1988).

(66) Maschio, L.; Kirtman, B.; Rérat, M.; Orlando, R.; Dovesi, R. *J. Chem. Phys.* **2013**, *139*, 164101.

(67) Maschio, L.; Kirtman, B.; Orlando, R.; Rérat, M. *J. Chem. Phys.* **2012**, *137*, 204113.

(68) Pascale, F.; Zicovich-Wilson, C. M.; Gejo, F. L.; Civalleri, B.; Orlando, R.; Dovesi, R. *J. Comput. Chem.* **2004**, *25*, 888.

(69) Zicovich-Wilson, C. M.; Pascale, F.; Roetti, C.; Saunders, V. R.; Orlando, R.; Dovesi, R. *J. Comput. Chem.* **2004**, *25*, 1873.

(70) Dashjav, E.; Tietz, F. *Z. anorg. allg. Chem.* **2014**, *640*, 3070.

(71) Loudon, R. *Adv. Phys.* **1964**, *13*, 423.

(72) Kosova, N. V.; Osintsev, D. I.; Uvarov, N. F.; Devyatkina, E. T. *Chem. Sustainable Devel.* **2005**, *13*, 253.

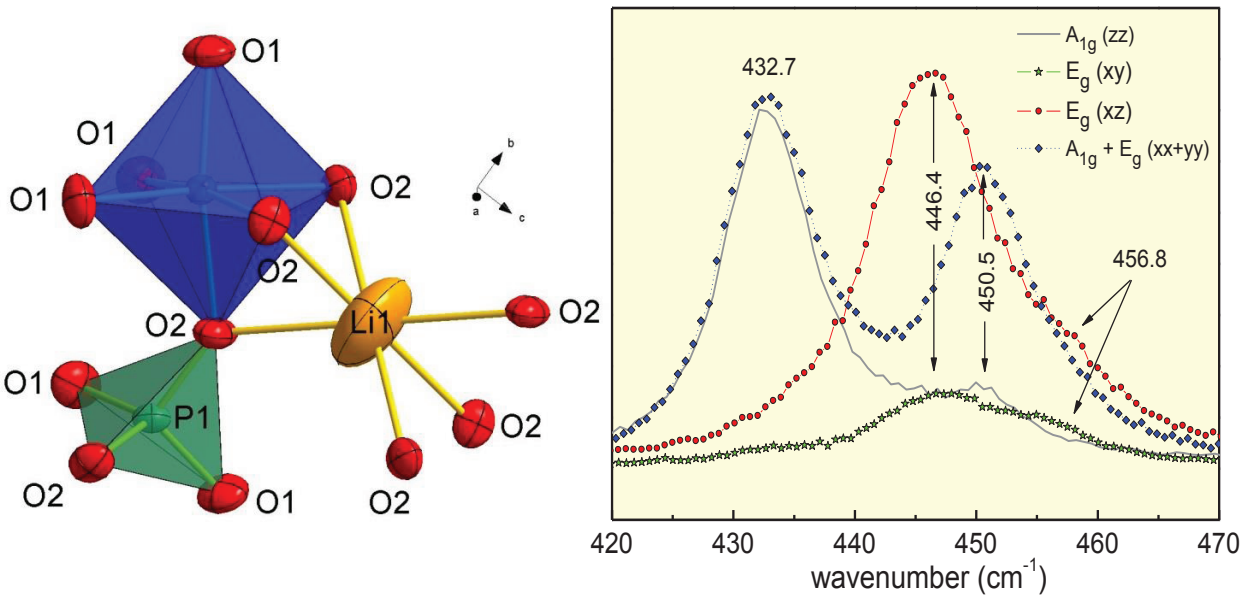


Figure 6: Graphical Abstract